

3D Antenna Radiation Pattern Reconstruction in a Reverberation Chamber Using Spherical Wave Decomposition

Qian Xu, Yi Huang, *Senior Member, IEEE*, Lei Xing, Chaoyun Song, *Student Member, IEEE*, Zhihao Tian, *Student Member, IEEE*, Saqer S. Alja'afreh and Manoj Stanley

Abstract—It has been shown that the correlation between the radiation patterns of two antennas can be measured in a reverberation chamber (RC). In this paper, it is shown that the self-correlation coefficient of an antenna, defined as the correlation between the radiation pattern of an antenna under test (AUT) and a transformed version of itself, can also be measured in an RC. It is found that the three-dimensional (3D) radiation pattern of the AUT can be reconstructed from the measured self-correlation coefficient by using spherical wave decomposition. Moreover, the axial ratio of the AUT can also be measured efficiently in the RC when the pattern is directional. Numerical simulations and measurements in the RC and in an anechoic chamber have been undertaken. Good agreement is obtained which confirms the validity of the proposed method. Thus this novel method can become a very useful, cost-effective and efficient method for 3D antenna radiation pattern measurement.

Index Terms—Antenna measurement, axial ratio, envelop correlation coefficient, antenna radiation pattern measurement, reverberation chamber.

I. INTRODUCTION

A REVERBERATION chamber (RC) has been proven to be an important and useful facility for measuring antenna properties, such as radiation efficiency [1-5], free-space impedance/*S*-parameters [6], and diversity gain [7-10]. However, it is not easy to measure the radiation pattern of an antenna in an RC because of multipath interference. It has been shown that by using a deconvolution technique [11], the radiation pattern of the antenna under test (AUT) can be reconstructed in a non-anechoic environment. It is also possible to measure the pattern directly in an RC when the line-of-sight (LoS) response dominates the unstirred part. In this case, the

Manuscript received Nov. 29, 2015. Corresponding author: Y. Huang. This work was supported in part by the National Natural Science Foundation of China (61601219) and Natural Science Foundation of Jiangsu Province (BK20160804).

Q. Xu and L. Xing are with College of Electronic and Information Engineering, Nanjing University of Aeronautics and Astronautics, Nanjing 211106, China (emxu@foxmail.com).

Y. Huang, C. Song, Z. Tian and M. Stanley are with the Department of Electrical Engineering and Electronics, The University of Liverpool, Liverpool, L69 3GJ, UK (e-mail: yi.huang@liv.ac.uk; sgcsong2@liv.ac.uk; zhihao.tian@liv.ac.uk; manoj.stanley@liv.ac.uk).

S. Alja'afreh is with the Electrical Engineering Department at Mu'tah University, Mu'tah, 61710, Jordan (e-mail: saqer1981@yahoo.com).

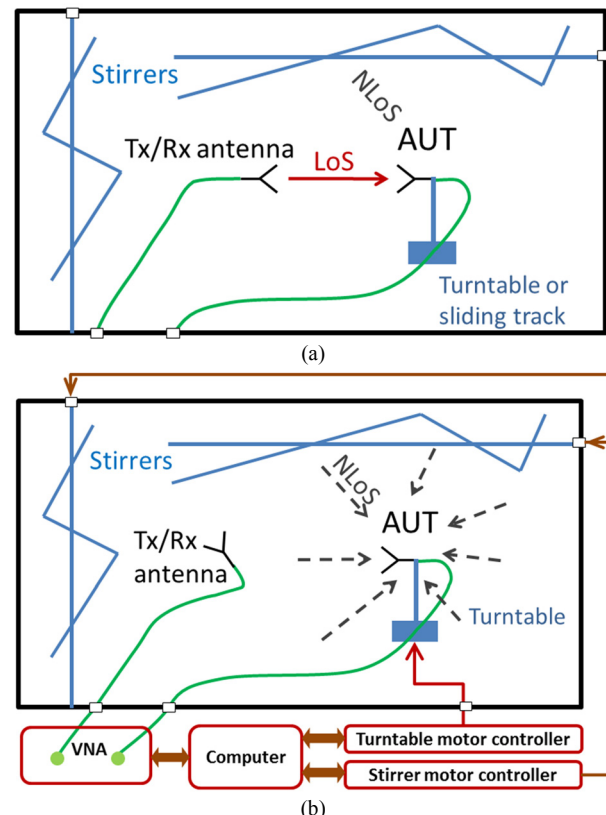


Fig. 1. Antenna radiation pattern measurement setup in the RC, (a) existing methods, (b) proposed method.

pattern can be extracted by using the *K*-factor [12-14] or Doppler shift [15-16]. A typical measurement setup is shown in Fig. 1(a) where two antennas are connected to the measurement instrument, a high directivity transmitting (Tx) or receiving (Rx) antenna is fixed and directed towards the AUT. The non-line-of-sight (NLoS) part can either be averaged out by rotating the stirrer [13, 14], or be filtered by using the Doppler shift (moving the AUT along a sliding track) [15, 16]. By rotating the turntable, the angle dependency of radiation pattern can be measured. That is, the information hidden behind the LoS/unstirred response is extracted while removing the NLoS/stirred response. It is also possible to extract the radiation pattern by using the time-reversal technique in the RC [17-19], but the time-reversal behavior of the RC need to be carefully characterized and calibrated.

In this paper, we propose a new method which can extract the 3D pattern of the AUT from the NLoS/stirred response while the LoS/unstirred response is not needed. This is very different from previous methods. The measurement setup is shown in Fig. 1(b) where the Tx/Rx antenna is not directed to the AUT. Since the RC is inherently a rich multipath environment, using the stirred part is actually easier than using the unstirred part. As can be seen later, the measurement time using the setup in Fig. 1(b) is comparable with the measurement time in an anechoic chamber (AC). In Fig. 1(a), the LoS/unstirred part needs to be extracted by rotating the stirrers or moving the AUT (along the sliding track) for each AUT angle, this could be very time consuming.

In the proposed method, the radiation pattern of the AUT is decomposed into spherical harmonics with unknown coefficients, and the pattern measurement becomes a generalized mode matching problem. By measuring the self-correlation coefficient of the radiation pattern in the RC, the coefficients of the spherical wave modes/harmonics can be inverted and thus the radiation pattern can be reconstructed.

The paper is organized in four sections. The theory is given in Section II where the forward problem and inverse problem are defined, and it is found that the axial ratio (AR) of the AUT can also be measured under a certain approximations. In Section III, simulations and measurements are conducted to verify the proposed method, results from the RC and AC are compared and good agreement is obtained. Finally, discussions and conclusions are presented in Section IV.

II. THEORY

In this section, we first explain the forward problem: if the radiation pattern of the antenna is already known, the self-correlation coefficient can be calculated. Then, the inverse problem is introduced to reconstruct the radiation pattern from the self-correlation coefficient. Finally, the expression for the axial ratio (AR) is derived under a certain approximation.

It is well-known that the far-field radiation pattern of an antenna can be decomposed into a superposition of spherical wave harmonics [20-24]. Two types of decomposition have been used: vector spherical harmonics (VSHs) with scalar coefficients and scalar spherical harmonics (SSHs) with vector coefficients. It has been shown that SSHs with vector coefficients can avoid the singularity problem of the antenna field on the poles [22-24], therefore we use SSHs with vector coefficients in this paper.

The far-field of an antenna can be expressed as [23]

$$\mathbf{E}(\theta, \varphi) = \lim_{L \rightarrow \infty} \sum_{l=0}^L \sum_{m=-l}^l \mathbf{a}_{lm} Y_l^m(\theta, \varphi) \quad (1)$$

where θ, φ are the polar angle and azimuthal angle in the spherical coordinate system respectively, $Y_l^m(\theta, \varphi)$ is the scalar spherical harmonic with level l and mode m defined by

$$Y_l^m(\theta, \varphi) = \sqrt{\frac{(2l+1)(l-m)!}{4\pi(l+m)!}} P_l^m(\cos\theta) e^{jm\varphi} \quad (2)$$

$P_l^m(\cos\theta)$ is the associated Legendre functions of the first kind [23]. The vector coefficients \mathbf{a}_{lm} can be obtained by using the orthogonality of the SSHs [22] with each component $a_{x,lm}$, $a_{y,lm}$ and $a_{z,lm}$, ($\mathbf{a}_{lm} = [a_{x,lm} \ a_{y,lm} \ a_{z,lm}]$), $\mathbf{E}(\theta, \varphi) = [E_x(\theta, \varphi) \ E_y(\theta, \varphi) \ E_z(\theta, \varphi)]$

$$a_{x,lm} = \int_0^{2\pi} \int_0^\pi E_x(\theta, \varphi) Y_l^{m*}(\theta, \varphi) \sin\theta \ d\theta \ d\varphi$$

$$a_{y,lm} = \int_0^{2\pi} \int_0^\pi E_y(\theta, \varphi) Y_l^{m*}(\theta, \varphi) \sin\theta \ d\theta \ d\varphi$$

$$a_{z,lm} = \int_0^{2\pi} \int_0^\pi E_z(\theta, \varphi) Y_l^{m*}(\theta, \varphi) \sin\theta \ d\theta \ d\varphi \quad (3)$$

where * means complex conjugate.

A. Forward Problem

If the far-field of the radiation pattern is known, using (3), the far-field can be decomposed into SSHs using (1) with a truncation of level L [23]. Suppose we have two antennas, where the radiation patterns are $\mathbf{E}_1(\theta, \varphi)$ and $\mathbf{E}_2(\theta, \varphi)$ respectively, the correlation coefficient ρ_E between these two antennas is [25, 26]

$$\rho_E = \frac{|\iint \mathbf{E}_1(\theta, \varphi) \cdot \mathbf{E}_2^*(\theta, \varphi) d\Omega|}{\sqrt{\iint |\mathbf{E}_1(\theta, \varphi)|^2 d\Omega} \sqrt{\iint |\mathbf{E}_2(\theta, \varphi)|^2 d\Omega}} \quad (4)$$

where $\iint \mathbf{E} d\Omega = \int_0^{2\pi} \int_0^\pi \mathbf{E} \sin\theta \ d\theta \ d\varphi$ means the integral over a unit spherical surface. Suppose that $\mathbf{E}_1(\theta, \varphi)$ and $\mathbf{E}_2(\theta, \varphi)$ are expanded by using the SSHs with order L

$$\begin{aligned} \mathbf{E}_1(\theta, \varphi) &= \sum_{l=0}^L \sum_{m=-l}^l \mathbf{a}_{lm} Y_l^m(\theta, \varphi) \\ \mathbf{E}_2(\theta, \varphi) &= \sum_{l=0}^L \sum_{m=-l}^l \mathbf{b}_{lm} Y_l^m(\theta, \varphi) \end{aligned} \quad (5)$$

Since the SSHs are orthogonal to each other on a unit spherical surface, substituting (5) into (4) gives the correlation coefficient

$$\rho_E = \frac{|\sum_{l=0}^L \sum_{m=-l}^l \mathbf{a}_{lm} \cdot \mathbf{b}_{lm}^*|}{\sqrt{\sum_{l=0}^L \sum_{m=-l}^l \|\mathbf{a}_{lm}\|^2} \sqrt{\sum_{l=0}^L \sum_{m=-l}^l \|\mathbf{b}_{lm}\|^2}} \quad (6)$$

Since $a_{x,lm}$, $a_{y,lm}$, and $a_{z,lm}$ are complex numbers, we use $\|\mathbf{a}_{lm}\|^2$ to represent the square of the magnitude of each coefficient, which is $\|\mathbf{a}_{lm}\|^2 = |a_{x,lm}|^2 + |a_{y,lm}|^2 + |a_{z,lm}|^2$.

Now we introduce the concept of the self-correlation

coefficient. Suppose $\mathbf{E}_2(\theta, \varphi)$ can be transformed from $\mathbf{E}_1(\theta, \varphi)$ by using rotations. That is, $\mathbf{E}_2(\theta, \varphi)$ is a transformed version of $\mathbf{E}_1(\theta, \varphi)$, they have the same shape but different reference coordinate systems. It should be noted that, to obtain a rotated version of $\mathbf{E}_1(\theta, \varphi)$, we only need to apply a rotation matrix to the coefficients at each level l [22, 27], which is

$$\begin{aligned} & [b_{x_{l,-l}} \cdots b_{x_{l,l}} \quad b_{y_{l,-l}} \cdots b_{y_{l,l}} \quad b_{z_{l,-l}} \cdots b_{z_{l,l}}] \\ & = [a_{x_{l,-l}} \cdots a_{x_{l,l}} \quad a_{y_{l,-l}} \cdots a_{y_{l,l}} \quad a_{z_{l,-l}} \cdots a_{z_{l,l}}] \mathbf{M}_l(\alpha, \beta, \gamma) \end{aligned} \quad (7)$$

where $\mathbf{M}_l(\alpha, \beta, \gamma)$ is the rotation matrix at level l ; (α, β, γ) means the pattern is rotated around x -axis first with angle α , then rotated around y -axis with angle β , and finally rotated around z -axis with angle γ all with the right-hand rule, which means $\mathbf{M}_l(\alpha, \beta, \gamma) = \mathbf{M}_l(\alpha, 0, 0) \mathbf{M}_l(0, \beta, 0) \mathbf{M}_l(0, 0, \gamma)$. Since the total radiated power of $\mathbf{E}_1(\theta, \varphi)$ and $\mathbf{E}_2(\theta, \varphi)$ are the same, we have $\sum_{l=0}^L \sum_{m=-l}^l |\mathbf{a}_{lm}|^2 = \sum_{l=0}^L \sum_{m=-l}^l |\mathbf{b}_{lm}|^2$, (6) becomes

$$\rho_{SC}(\alpha, \beta, \gamma) = \frac{|\sum_{l=0}^L \sum_{m=-l}^l \mathbf{a}_{lm} \cdot T_{\alpha\beta\gamma}^*(\mathbf{a}_{lm})|}{\sum_{l=0}^L \sum_{m=-l}^l \|\mathbf{a}_{lm}\|^2} \quad (8)$$

which is the definition of the *self-correlation* coefficient (ρ_{SC}), where we use $T_{\alpha\beta\gamma}(\mathbf{a}_{lm})$ to represent the transformed version of \mathbf{a}_{lm} by using (7). Since $T_{\alpha\beta\gamma}$ depends on the rotation angles, ρ_{SC} is also a function of rotation angles.

As expected, the forward problem is well-defined, once the radiation pattern of the antenna $\mathbf{E}_1(\theta, \varphi)$ is known, the self-correlation coefficient can be calculated using (7) and (8). The calculation procedure for the rotation matrix $\mathbf{M}_l(\alpha, \beta, \gamma)$ can be found in [22, 27].

B. Inverse Problem

If the angle dependency of ρ_{SC} in (8) is known, by solving (8) for \mathbf{a}_{lm} , the 3D radiation pattern of the AUT can be reconstructed. As can be seen, the inverse problem is actually a generalized mode matching problem, that is, the coefficients of the spherical wave modes need to be solved to match the angle dependency of ρ_{SC} .

Luckily, this self-correlation coefficient can be measured in the RC using the setup as shown in Fig. 1(b). The measurement procedure is very similar to the diversity gain measurement [7-10], the only difference is: in the diversity gain measurement, $\mathbf{E}_1(\theta, \varphi)$ and $\mathbf{E}_2(\theta, \varphi)$ in (4) are the radiation pattern of the two multiple-input multiple-output (MIMO) antenna branches; in this measurement, $\mathbf{E}_2(\theta, \varphi)$ is a rotated version of $\mathbf{E}_1(\theta, \varphi)$. We just need to rotate the AUT for a set of angles (α, β, γ) instead of switching the receiving/transmitting port in the diversity gain measurement.

The correlation coefficient can be obtained by measuring the S -parameters in the RC [25, 26, 28]

$$\rho_S(\alpha, \beta, \gamma) = \text{corr}(S_{31}, S_{32})$$

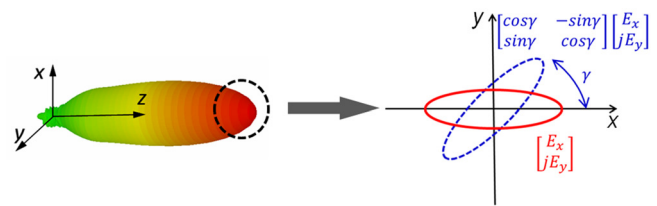


Fig. 2. Self-correlation of a directional antenna, the integral result is dominated by the field in the main beam direction.

$$= \frac{|\sum_{k=1}^N (S_{31}(k) - \langle S_{31} \rangle) (S_{32}(k) - \langle S_{32} \rangle)^*|}{\sqrt{\sum_{k=1}^N |S_{31}(k) - \langle S_{31} \rangle|^2 \sum_{k=1}^N |S_{32}(k) - \langle S_{32} \rangle|^2}} \quad (9)$$

where N represents the total number of samples collected, $\langle \cdot \rangle$ means the average value of N samples. In the diversity gain measurement, S_{31} and S_{32} represent the measured S -parameters between the Tx/Rx antenna (in Fig. 1(b)) and two MIMO branches respectively. In this measurement, S_{31} and S_{32} represent the measured S -parameters between the Tx/Rx antenna and AUT at two different positions respectively. Since position 2 is the same antenna rotated from position 1, and it has been shown that the correlation of measured S -parameters equals the correlation of the radiation patterns [25, 26], thus we have

$$\rho_S(\alpha, \beta, \gamma) = \rho_{SC}(\alpha, \beta, \gamma) \quad (10)$$

To solve \mathbf{a}_{lm} , two more conditions are needed: the radiated power should be normalized to 1 (otherwise \mathbf{a}_{lm} can be scaled arbitrarily), and the far-field condition should be satisfied. This is because we use the SSHs rather than VSHs, while in the VSHs, the far-field condition can be satisfied automatically (but the singularity problem needs to be treated separately [22]). Mathematically, these two conditions are

$$\sum_{l=0}^L \sum_{m=-l}^l \|\mathbf{a}_{lm}\|^2 = 1 \quad (11)$$

$$\hat{\mathbf{r}}(\theta, \varphi) \cdot \sum_{l=0}^L \sum_{m=-l}^l \mathbf{a}_{lm} Y_l^m(\theta, \varphi) = 0 \quad (12)$$

where $\hat{\mathbf{r}}(\theta, \varphi)$ is the unit vector in radial direction.

As can be seen, the inverse problem is a generalized mode matching problem defined by the nonlinear equation system (10) - (12), and these can be solved numerically by using the Levenberg-Marquardt algorithm [29] as shown later in this paper.

C. Axial Ratio

It is interesting to note that, under certain approximations, the problem can be simplified. If the antenna is a directional antenna, the integral in (4) can be approximately evaluated using the field in the main beam as shown in Fig. 2. Suppose that the main beam is aligned with z -axis and rotated around it by an angle γ . The integral (4) can be approximated as

$$\rho_{SC}(\gamma) = \frac{|\iint \mathbf{E}_1(\theta, \varphi) \cdot \mathbf{E}_2^*(\theta, \varphi) d\Omega|}{\sqrt{\iint |\mathbf{E}_1(\theta, \varphi)|^2 d\Omega \iint |\mathbf{E}_2(\theta, \varphi)|^2 d\Omega}}$$

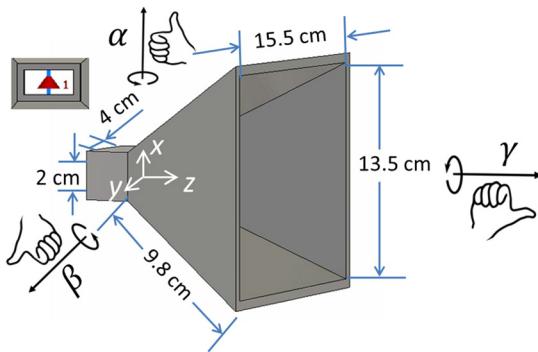


Fig. 3. The dimensions of the horn antenna and the definition of the rotation angles α , β , γ and axes x , y , z . The antenna is excited by using a lumped port located at the center of the waveguide.

$$\begin{aligned} & \approx \left| \frac{\begin{bmatrix} \cos\gamma & -\sin\gamma \\ \sin\gamma & \cos\gamma \end{bmatrix} \begin{bmatrix} E_x \\ jE_y \end{bmatrix} \cdot \begin{bmatrix} E_x \\ jE_y \end{bmatrix}^*}{E_x^2 + E_y^2} \right| \\ & = \frac{|(E_x^2 + E_y^2)\cos\gamma - 2jE_xE_y\sin\gamma|}{E_x^2 + E_y^2} \end{aligned} \quad (13)$$

where $\mathbf{E}_1(\theta, \varphi)$ is the original pattern, $\mathbf{E}_2(\theta, \varphi)$ is the rotated pattern with angle γ . It can be found from (13) that, when $\gamma = 90^\circ$ the $\rho_{SC}(\gamma)$ has the minimum value

$$\rho_{SC}(\gamma)_{min} \approx \frac{2E_xE_y}{E_x^2 + E_y^2} \quad (14)$$

Note that the AR is defined as E_x/E_y , thus the minimum of $\rho_{SC}(\gamma)$ can be related to the AR of the antenna

$$\begin{aligned} \rho_{SC}(\gamma)_{min} & \approx \frac{2E_xE_y}{E_x^2 + E_y^2} = \frac{2(E_x/E_y)}{1 + (E_x/E_y)^2} = \frac{2(E_y/E_x)}{1 + (E_y/E_x)^2} \\ & = \frac{2AR}{1 + AR^2} \end{aligned} \quad (15)$$

and the AR can be obtained from

$$AR \approx \frac{1 + \sqrt{1 - \rho_{SC}^2(\gamma)_{min}}}{\rho_{SC}(\gamma)_{min}} \quad (16)$$

This offers an opportunity to measure the AR in the RC for directional antennas.

III. SIMULATIONS AND MEASUREMENTS

In this section, simulations and measurements are conducted to verify the proposed method. Before conducting the measurements, numerical simulations are carried out. Since in the numerical simulation, once the geometrical structure of the AUT is defined, the radiation pattern of the AUT can be obtained by using the full wave simulation software (CST Microwave Studio is used in this paper). Thus the simulated radiation pattern can be used as the reference, and we can

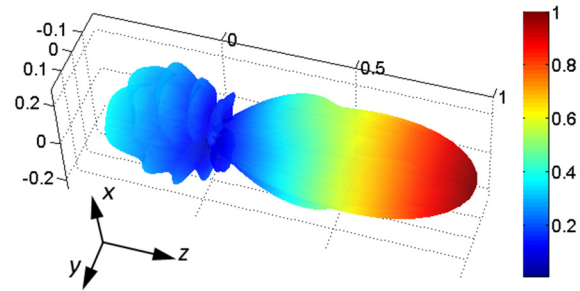


Fig. 4. The simulated E-field magnitude pattern (linear scale) at 5 GHz, the maximum value is normalized to 1 V/m.

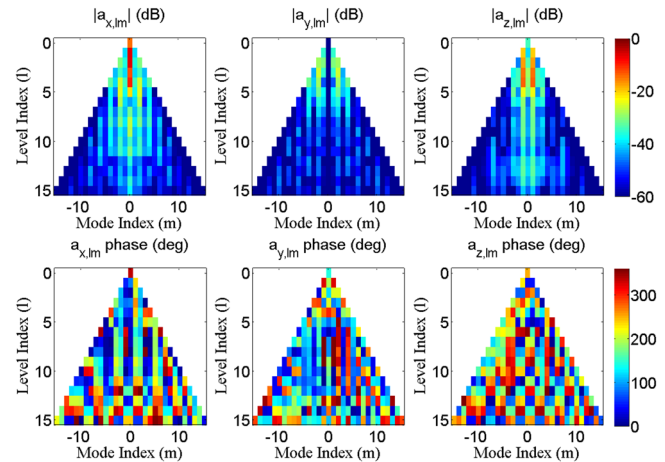


Fig. 5. The decomposed magnitude (dB scale, $20\log|a_{lm}|$) and phase (degree) of the SSHs of the radiation pattern in Fig. 4, a_{lm} is normalized to make sure $\sum_{l=0}^L \sum_{m=-l}^l \|a_{lm}\|^2 = 1$.

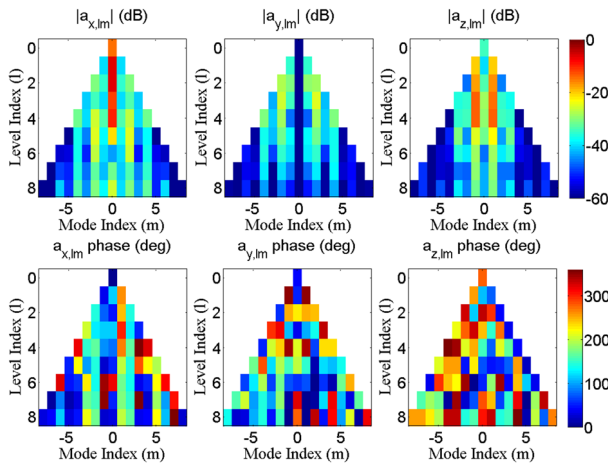
compare the reconstructed pattern (obtained from the self-correlation coefficients) with the pattern obtained by using CST to verify the proposed method. Then measurements in the RC and AC are conducted and the results are compared. We use the measured results obtained in AC as the reference to confirm the effectiveness of the proposed method.

A. Simulations

A typical rectangular horn antenna shown in Fig. 3 is used as the AUT in the numerical simulation. The definitions of the rotation angles are also given (right-hand rule). The simulated radiation pattern at 5 GHz is obtained by using CST Microwave Studio and given in Fig. 4 with maximum E-field magnitude normalized to 1V/m.

The radiation pattern can be decomposed into SSHs with coefficients a_{lm} (the forward problem) by using (3). The magnitude and phase of each component of a_{lm} are shown in Fig. 5. We use L up to 15 in Fig. 5, as can be seen, when $l > 8$, the magnitude of the SSHs is already very small (< -27 dB). Then, (8) is used to obtain the self-correlation coefficients of the radiation pattern, since the AUT is rotated only around the x -, y -, and z -axes, we use $\rho_{SC}(\alpha)$, $\rho_{SC}(\beta)$ and $\rho_{SC}(\gamma)$ instead of $\rho_{SC}(\alpha, 0, 0)$, $\rho_{SC}(0, \beta, 0)$ and $\rho_{SC}(0, 0, \gamma)$ respectively.

After the self-correlation coefficients of the radiation pattern are obtained, the radiation pattern of the AUT can be reconstructed (the inverse problem). Mathematically, by combining (10), (11) and (12), the inverse problem can be expressed as

Fig. 6. Reconstructed \mathbf{a}_{lm} from (17).

$$\left\{ \begin{array}{l} \frac{|\sum_{l=0}^L \sum_{m=-l}^l \mathbf{a}_{lm} \cdot T_{\alpha}^*(\mathbf{a}_{lm})|}{\sum_{l=0}^L \sum_{m=-l}^l \|\mathbf{a}_{lm}\|^2} = \rho_{SC}(\alpha), \quad \alpha = 1, 2, \dots, 360^\circ \\ \frac{|\sum_{l=0}^L \sum_{m=-l}^l \mathbf{a}_{lm} \cdot T_{\beta}^*(\mathbf{a}_{lm})|}{\sum_{l=0}^L \sum_{m=-l}^l \|\mathbf{a}_{lm}\|^2} = \rho_{SC}(\beta), \quad \beta = 1, 2, \dots, 360^\circ \\ \frac{|\sum_{l=0}^L \sum_{m=-l}^l \mathbf{a}_{lm} \cdot T_{\gamma}^*(\mathbf{a}_{lm})|}{\sum_{l=0}^L \sum_{m=-l}^l \|\mathbf{a}_{lm}\|^2} = \rho_{SC}(\gamma), \quad \gamma = 1, 2, \dots, 360^\circ \\ \sum_{l=0}^L \sum_{m=-l}^l \|\mathbf{a}_{lm}\|^2 = 1, \\ \hat{\mathbf{r}}(\theta, \varphi) \cdot \sum_{l=0}^L \sum_{m=-l}^l \mathbf{a}_{lm} Y_l^m(\theta, \varphi) = 0, \quad (\theta, \varphi) \in \mathbb{S} \end{array} \right. \quad (17)$$

where $L = 8$ is chosen, $\rho_{SC}(\alpha)$, $\rho_{SC}(\beta)$ and $\rho_{SC}(\gamma)$ are sampled at 1 degree/step, \mathbb{S} is the point set chosen on the sphere, 5 degree/step is used for both θ and φ angles.

The nonlinear system of equations (17) can be solved/optimized using the Levenberg-Marquardt algorithm [29] in Matlab. After optimization, the reconstructed \mathbf{a}_{lm} are obtained and shown in Fig. 6. As can be seen, compared with Fig. 5, they have a very similar magnitude but different phase, which is not an issue since the phase is a relative value. The reconstructed ρ_{SC} calculated from the reconstructed \mathbf{a}_{lm} are shown in Fig. 7, comparisons between the reconstructed ρ_{SC} and ρ_{SC} of the original pattern (Fig. 4) are shown. As can be seen, a very good agreement has been obtained except at some angles. The 3D radiation pattern can be obtained quickly using $\mathbf{E}(\theta, \varphi) = \sum_{l=0}^L \sum_{m=-l}^l \mathbf{a}_{lm} Y_l^m(\theta, \varphi)$ and is shown in Fig. 8. Compared with Fig. 4, a very similar pattern is reconstructed. Comparisons of co-polarization and cross-polarization components in the YOZ plane and the relative error in all angles are given in Fig. 9. As can be seen, a good agreement is obtained in the main lobe of the pattern. However, the back lobe, side lobe and the cross-polarization component are not exactly the same, which will be discussed in the next section.

The AR measurement result in the RC can also be verified through simulation. We use a conical horn antenna with two

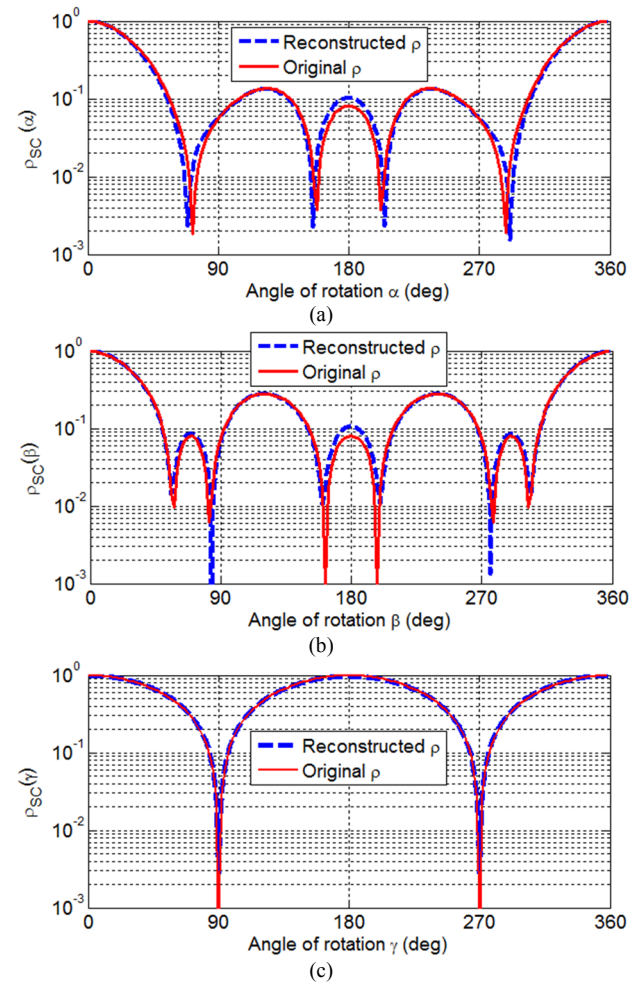
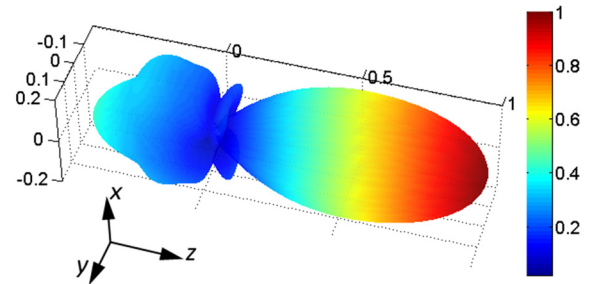
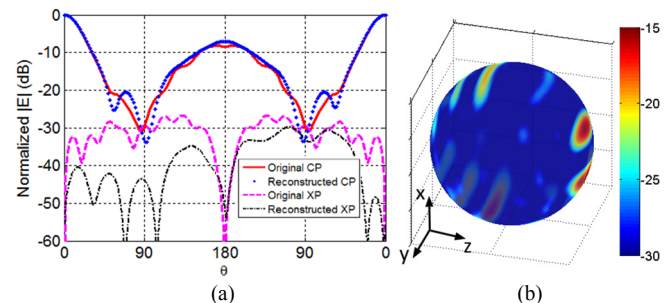
Fig. 7. Reconstructed ρ_{SC} and the original ρ_{SC} . (a), (b) and (c) are the self-correlation rotated around x-, y- and z-axis respectively.

Fig. 8. Reconstructed E-field magnitude pattern (linear scale) at 5 GHz, the maximum value is normalized to 1 V/m.

Fig. 9. (a) Co-polarization (CP) and cross-polarization (XP) of the original pattern (Fig. 4) and the reconstructed pattern (Fig. 8) in YOZ plane, normalized to the peak value in dB; (b) $20\log\|\mathbf{E}\| - \|\mathbf{E}'\|$, relative error in all angles in dB, where \mathbf{E} and \mathbf{E}' are the original pattern (Fig. 4) and the reconstructed pattern (Fig. 8) respectively (\mathbf{E} and \mathbf{E}' are normalized to the peak value of 1V/m).

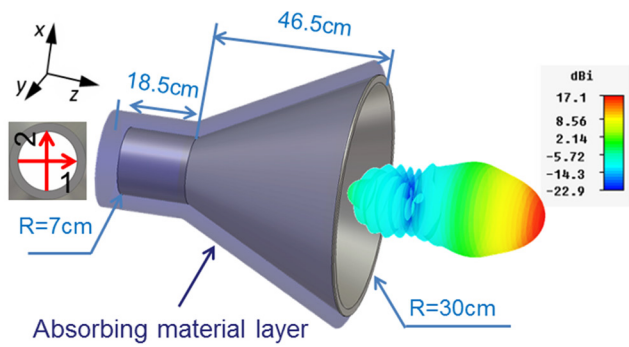


Fig. 10. The conical antenna and a typical radiation pattern at 1.5 GHz, two perpendicular lumped ports are used to synthesize waves with different AR values.

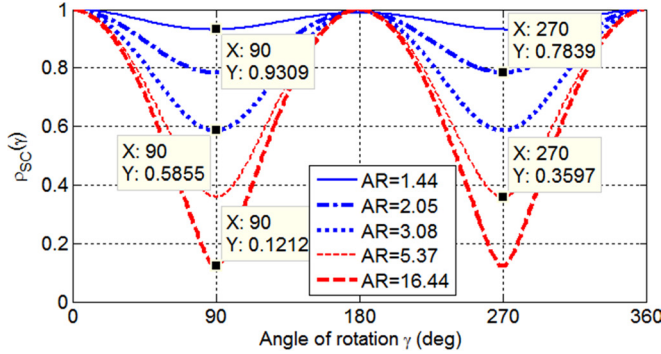


Fig. 11. $\rho_{sc}(\gamma)$ with different AR values, the AR values in the legend are read from CST directly.

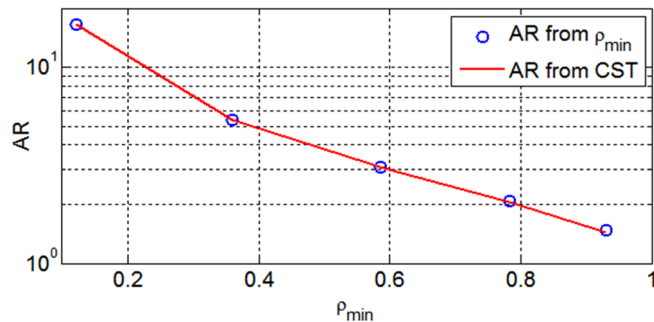


Fig. 12. AR obtained from $\rho_{sc}(\gamma)_{min}$ using (16) and AR obtained from CST.

perpendicular excited ports to generate a directional pattern with different AR values. To improve the radiation pattern, a layer of absorbing material is used to suppress the side lobe and back lobe. The model is shown in Fig. 10, by tuning the phase difference between port 1 and port 2, waves with different AR can be simulated.

Patterns with different AR values are generated and decomposed into SSHs with \mathbf{a}_{lm} , thus $\rho_{sc}(\gamma)$ can be obtained by using (8) with different rotation angles. Results are given in Fig. 11 with minimum value markers. Finally, (16) is used to extract the AR values from $\rho_{sc}(\gamma)_{min}$ and compared with the AR values obtained from CST (shown in Fig. 12). As can be seen, a very good agreement is obtained.

B. Measurements

Measurements were conducted in the AC and RC at the University of Liverpool, the radiation pattern measurement setup in the AC is shown in Fig. 13, the SATIMO® SH 2000

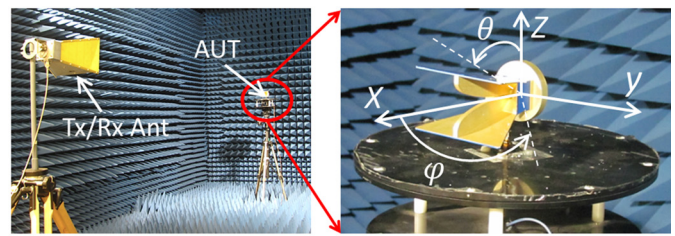


Fig. 13. Radiation pattern measurement in the AC and the definition of x-, y-, and z-axis.

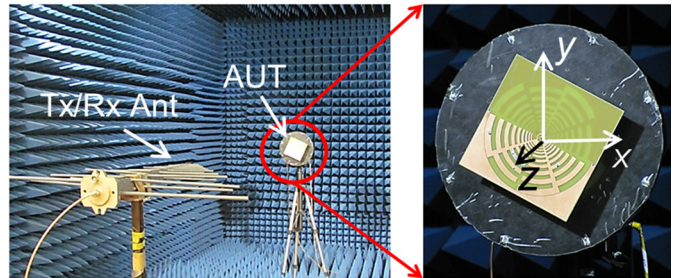


Fig. 14. AR measurement in the AC.

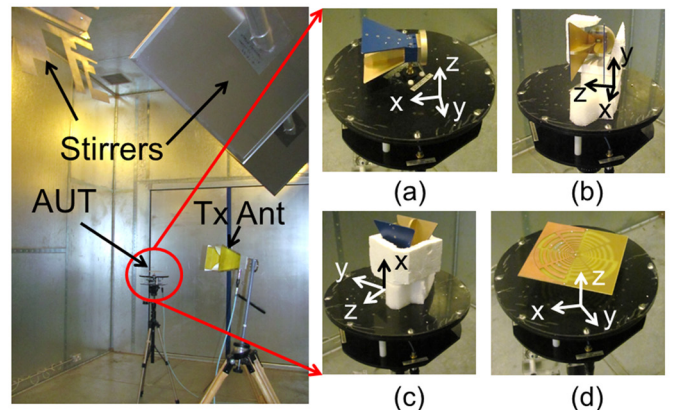


Fig. 15. Measurement setup in the RC, AUT rotated around z-, y-, and x-axis are shown in (a), (b) and (c) respectively, AR measurement is shown in (d).

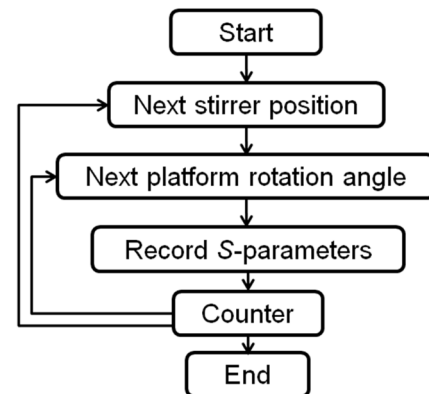


Fig. 16. Self-correlation measurement flowchart in the RC.

horn antenna was used as the AUT. In the AR measurement, we used a homemade wide band log-periodic cross dipole as the AUT (Fig. 14). Measurement setup in the RC is also shown in Fig. 15, foams were used to hold the AUT for three different rotation axes. The measurement scenarios and procedures were the same for different AUTs and different rotation axes.

In the pattern reconstruction, the procedure was the same as in the simulation, the only difference was that, $\rho_{sc}(\alpha)$, $\rho_{sc}(\beta)$

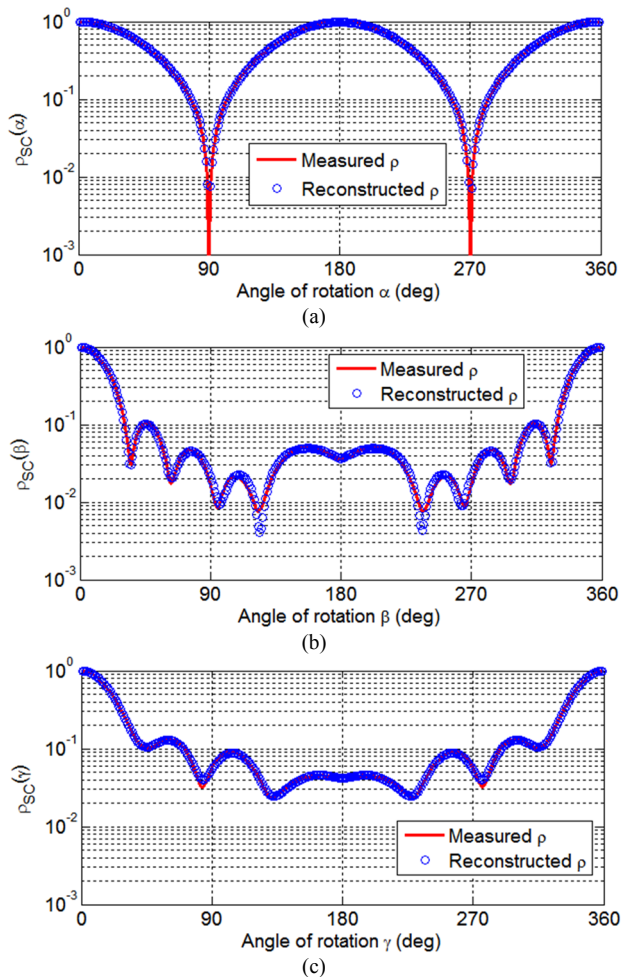


Fig. 17. Measured and reconstructed ρ_{SC} of the AUT (SATIMO® SH 2000), (a), (b) and (c) are the self-correlation rotated around x -, y - and z -axis respectively, the definition of three axes are shown in Fig. 13.

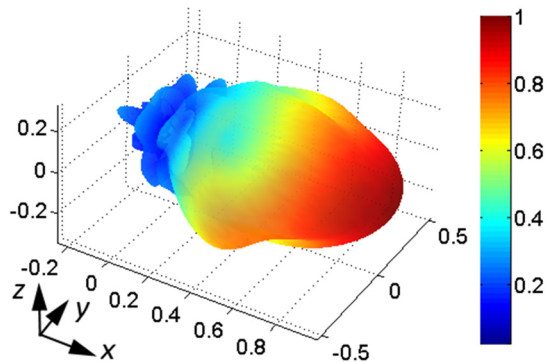


Fig. 18. Reconstructed E-field magnitude pattern (linear scale) of the AUT (SATIMO® SH 2000), the maximum value is normalized to 1 V/m.

and $\rho_{SC}(\gamma)$ were measured in the RC rather than simulated. The self-correlation coefficients were measured at 4 GHz with 50 points of frequency stir (in 10 MHz bandwidth), the turntable was rotated with 1 degree/step for 360 degrees and the stirrers were rotated with 3 stirrer positions. Therefore, we had frequency stir [30], source stir [31-33] and mechanical stir for each rotation angle, and $N = 50 \times 360 \times 3 = 54000$ sample points in (9) for each angle of self-correlation coefficient calculation. It should be noted that, the turntable and the stirrer were not rotated simultaneously. When the turntable was

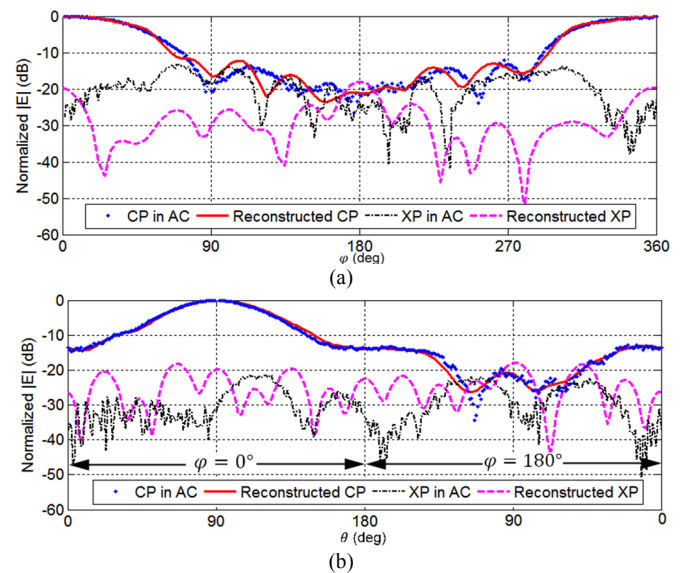
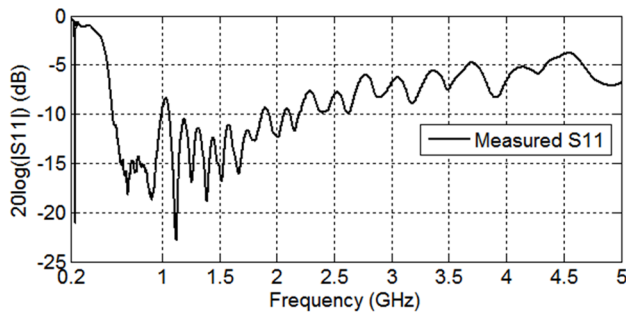
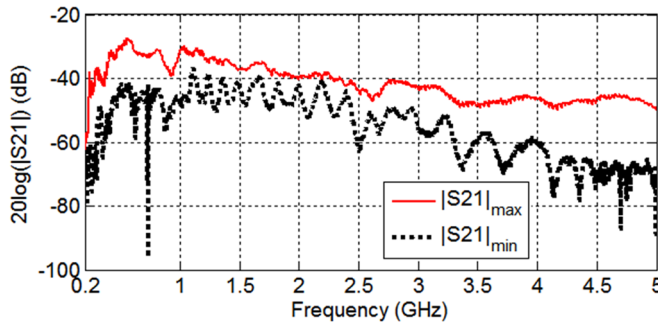
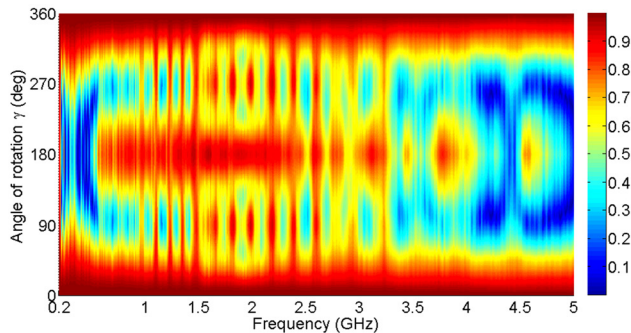
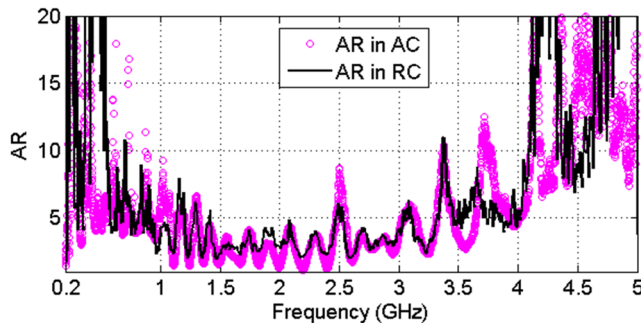


Fig. 19. Measured and reconstructed radiation pattern in XOY and XOZ plane, peak value is normalized to 0 dB, CP means co-polarization component, XP means cross-polarization component, (a) radiation pattern in XOY plane, (b) radiation pattern in XOZ plane.

rotated for a full revolution, the stirrer position was fixed at one position to make sure the environment was the same (shown in Fig. 16), and we assumed that the size of the antenna was not so large that rotating the antenna would perturb the field in the RC greatly, otherwise the results would be decorrelated and always gave small ρ_S . After all the S -parameters were collected, (9) was used to obtain the self-correlation coefficient for different angles of α , β , and γ .

The measured ρ_{SC} are shown in Fig. 17, and the reconstructed ρ_{SC} from \mathbf{a}_{lm} are also given. As expected they agree well with the measured results. The reconstructed 3D pattern from \mathbf{a}_{lm} by using the summation of SSHs is also shown in Fig. 18. To validate the results, the pattern in the XOY plane and the XOZ plane were also measured in the AC, results are compared in Fig. 19. As can be seen, very good agreement is obtained for the main beam; however, the error becomes large when the magnitude of the pattern becomes small (side lobes, back lobes and cross-polarization). The maximum error for the co-polarization component in the XOY plane occurs at $\theta = 90^\circ, \varphi = 252^\circ$ where the measured value is -23.8 dB and the reconstructed value is -15.0 dB. In the XOZ plane, the maximum error for the co-polarization component occurs at $\theta = 113^\circ, \varphi = 180^\circ$ where the measured value is -34.4 dB and the reconstructed value is -26.1 dB. This phenomenon is very similar to that in the numerical simulation and will be discussed in the next section.

In the AR measurement in Fig. 14, the AUT (the measured S11 is given in Fig. 20) was rotated on the turntable with 1 degree/step in the frequency range from 200 MHz to 5 GHz, S -parameters were collected for each degree between the AUT and the Tx antenna, the maximum and minimum values in a revolution are shown in Fig. 21. The AR values can be obtained using [34]

Fig. 20. Measured S_{11} of the AUT (wide band log-periodic cross dipole).Fig. 21. Measured maximum and minimum $|S_{21}|$ in a revolution in the AC.Fig. 22. Measured $\rho_{SC}(\gamma)$ at all frequencies in the RC (linear scale).Fig. 23. Measured $\rho_{SC}(\gamma)$ at all frequencies in the RC (linear scale). The directivity in 1 GHz ~ 3.5 GHz is about 5 dBi ~ 6.5 dBi.

$$AR = \frac{|S_{21}|_{max}}{|S_{21}|_{min}} \quad (18)$$

Similarly, the AR measurement was conducted in the RC using (16), measured $\rho_{SC}(\gamma)$ in the RC are shown in Fig. 22 at each frequency and the minimum values were extracted to calculate the AR. Finally, the obtained AR in the AC and RC are shown in Fig. 23, as can be seen, a very good agreement is obtained when the AUT is close to the circular polarization (1 GHz ~ 3.5 GHz).

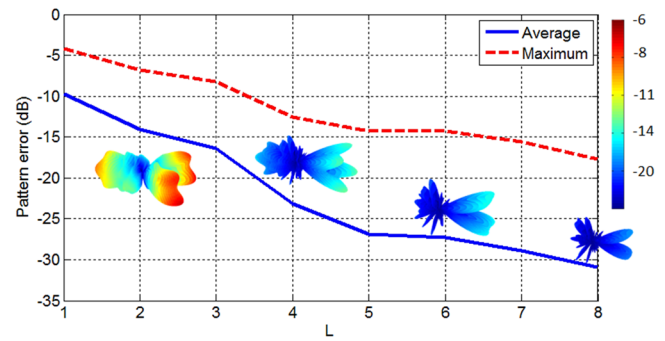


Fig. 24. Average and maximum pattern error with different L , the average error is defined as $20\log(\text{mean}||\mathbf{E}| - |\mathbf{E}'||)$ and the maximum error is defined as $20\log(\text{max}||\mathbf{E}| - |\mathbf{E}'||)$, where \mathbf{E} and \mathbf{E}' are the original pattern and the pattern approximated by using SSHs respectively (\mathbf{E} and \mathbf{E}' are normalized to the peak value of 1V/m, mean and max means obtaining the average and maximum value over all angles respectively; the error patterns ($20\log||\mathbf{E}| - |\mathbf{E}'||$) are also given when $L = 2, 4, 6, 8$.

IV. DISCUSSION

It should be noted that, in both simulation and measurements, the reconstructed patterns are similar to the original pattern but not exactly the same (Fig. 8 and Fig. 18), possible error sources and error analysis are discussed in this section.

1) The SSHs are truncated at level L . To analyze the error caused by L , different L are used to decompose the far-field in Fig. 4, by comparing the far-field calculated from \mathbf{a}_{lm} in (1) with the original pattern, the truncation effect is shown in Fig. 24, both average error and maximum error are given. As can be seen, for the antenna pattern in Fig. 4, when $L = 8$, the average pattern error is quite small.

2) The inverse problem is a complex nonlinear problem and could have multiple solutions. ρ_{SC} for all α, β, γ angles in Fig. 5 and Fig. 6 can be calculated using (8) and is shown in Fig. 25. In the measurements, because of the limitation of the facility, only three cut planes were measured which correspond to the values on the three axes in Fig. 25 ($\alpha = 1^\circ \sim 360^\circ, \beta = 0, \gamma = 0$; $\alpha = 0, \beta = 1^\circ \sim 360^\circ, \gamma = 0$; $\alpha = 0, \beta = 0, \gamma = 1^\circ \sim 360^\circ$). As can be seen, at some regions these two ρ_{SC} are different, which means that it could be possible to have two sets of ρ_{SC} with the same value on three axes but have differences in some regions. To quantify the relation between the pattern error and the error in the self-correlation coefficients, ρ_{SC} was perturbed with random values 2000 times. The pattern error was calculated in each case. Results are given in Fig. 26 which shows a direct statistical understanding between the error in ρ and the error in the pattern. It can be seen that, when the reconstructed ρ is accurate, statistically it is more likely to get a more accurate pattern. It is also possible to sample $\rho_{SC}(\alpha, \beta, \gamma)$ in 3D to reconstruct the radiation pattern. To simulate this procedure, the original $\rho_{SC}(\alpha, \beta, \gamma)$ in Fig. 25(a) was sampled in 3D with different degrees per step for all α, β , and γ . Using the resampled ρ_{SC} to reconstruct the pattern, the pattern errors with different step size can be obtained and are shown in Fig. 27. As expected, more 3D samples can improve the accuracy of the reconstructed pattern, but more time is needed in the optimization.

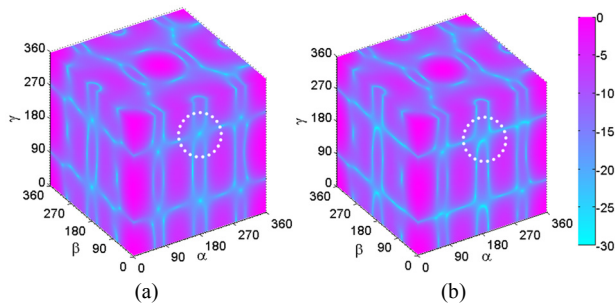


Fig. 25. Calculated $\rho_{SC}(\alpha, \beta, \gamma)$ from (a) original \mathbf{a}_{tm} in Fig. 5 and (b) reconstructed \mathbf{a}_{tm} in Fig. 6, a different region is marked with dotted circle (the color represents the value of $10\log\rho_{SC}(\alpha, \beta, \gamma)$, dB scale).

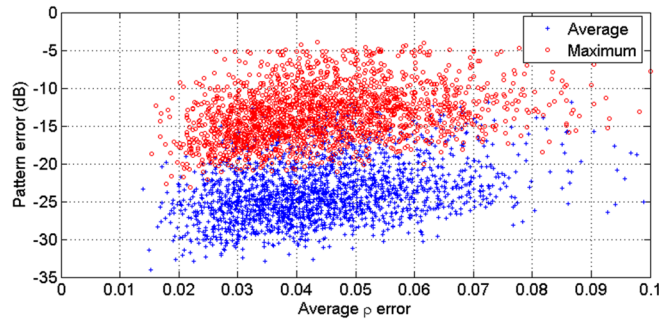


Fig. 26. The average ρ error (averaged over all selected sample angles) and the pattern error in dB: the average error is defined as $20\log(\text{mean}(|\mathbf{E}| - |\mathbf{E}'|))$ and the maximum error is defined as $20\log(\text{max}(|\mathbf{E}| - |\mathbf{E}'|))$, where \mathbf{E} and \mathbf{E}' are the original pattern and the reconstructed pattern respectively (\mathbf{E} and \mathbf{E}' are normalized to the peak value of 1V/m); *mean* and *max* means the average and maximum value over all angles respectively.

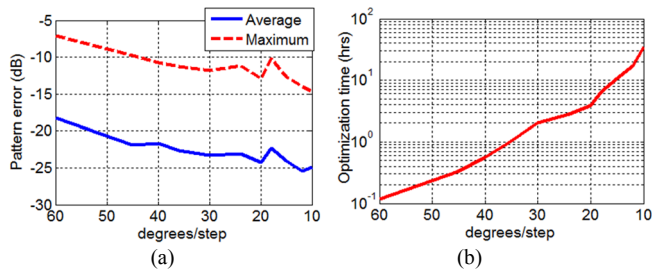


Fig. 27. (a) Typical reconstructed pattern error and the step size of 3D (α, β, γ) , e.g. 10 degrees/step means all α, β and γ are sampled every 10 degrees in the range of 0° to 360° , thus has 37 samples in each angle dimension and 50653 samples in total. Definitions of *average* and *maximum* are the same as in Fig. 26; (b) optimization time in hours for different degrees/step, the results are based on the same initial values and convergence tolerance in the Levenberg-Marquardt algorithm.

3) The inverse problem is a multi-goal optimization problem, the reconstruction accuracy is limited by the Levenberg-Marquardt algorithm; the optimized \mathbf{a}_{tm} could be at a local minimum rather than the global minimum. Normally, the main beam with co-polarization has the highest magnitude thus has higher weight than the other components (side lobes, back lobes, cross-polarizations, etc.).

4) To investigate the convergence of ρ , different sample numbers are used to repeat the calculation. The average ρ error with different sample numbers is shown in Fig. 28. As can be seen, when the sample number is large the measured ρ converges with small uncertainties.

Although the reconstructed pattern in the RC is not as accurate as that measured in the AC, an RC is more

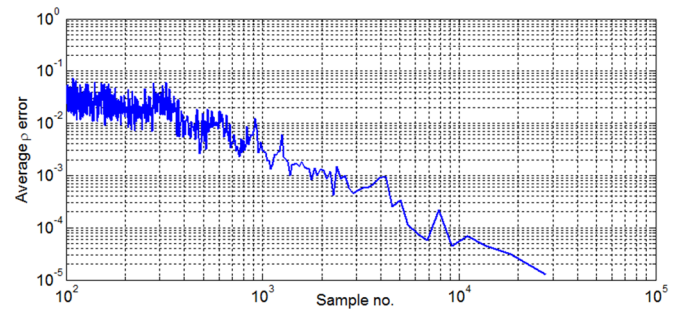


Fig. 28. The average ρ error (averaged over all selected sample angles) and the sample number, ρ values with 54000 samples are used as the reference.

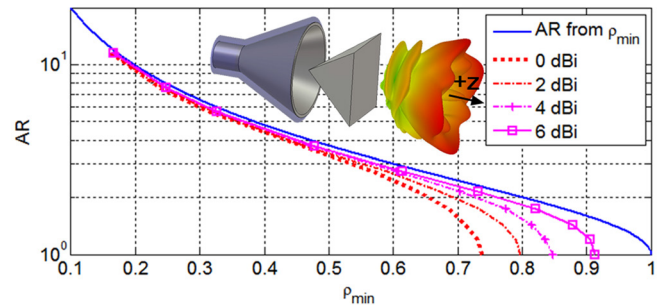


Fig. 29. Degradation curves with different directivity, AR curves deviate (16) (AR from ρ_{min}) when directivity reduces in +z direction.

cost-effective than an AC. There are also other advantages. For example, the proposed method can be conducted in 2D while the reconstructed radiation pattern is always in 3D. The proposed method is based on the NLoS/stirred part of the measured S -parameters. The AUT and the Tx/Rx antenna do not need to be carefully aligned as they would need to be in the AC, which makes the measurement setup more robust and insensitive to antenna positions. The measurement time is shorter than some of the methods using the LoS/unstirred part [13-16] (at each angle, the stirred part needs to be cancelled out by averaging S -parameters at many stirrer positions or using the Doppler shift). The measurement time could be even shorter than the direct measurement of the 3D radiation pattern in the AC with an acceptable loss of accuracy, since 3D sample points could be much larger than 2D sample points. Also, more time is needed in the post processing of the measurement data.

The AR of a directional antenna has also been measured approximately in the RC. This is under the assumption that the pattern integral is dominated by the main beam in (13). To investigate how the accuracy degrades over the directivity, we use a pyramid to block the wave in +z direction. By tuning the size of the pyramid we can tune the directivity but not change the AR in +z direction. Results with different directivity are shown in Fig. 29. As can be seen, even when the directivity is 0 dBi at +z direction, the maximum error of AR in (16) is 1.3. Therefore (16) is a very good approximation and different antenna may have different degradation curves.

It is also interesting to note that, by combing the existing measurement methods in the RC, with the same measurement setups but different data post-processing techniques, nearly all antenna parameters (such as radiation efficiency [1], 3D pattern in this paper, S_{11} [6] and gain) can be obtained in one measurement.

There are also potential issues: when the directivity of the

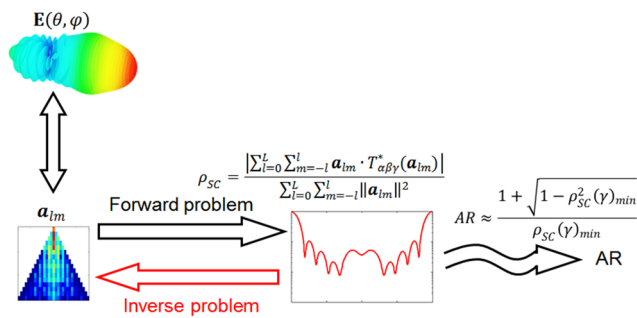


Fig. 30. An overview of the framework in this paper.

AUT is high (e.g. a parabolic antenna with a large reflector), ρ_{sc} becomes uncorrelated very quickly, and a very fine rotation step for the turntable is needed which could be time consuming for a whole revolution. Also, to approximate a high directivity pattern, more coefficients are required [35], which further increases the optimization time when solving (17), and the unknown numbers increase quickly at the order of $O(L^2)$. For $L = 8$ in this paper, the optimization time is around 2 hours on a personal computer. How to quickly reconstruct \mathbf{a}_{lm} of high directivity antenna could be challenging.

V. CONCLUSIONS

The concept of the self-correlation coefficient has been introduced in this paper. It has been shown for the first time that the 3D radiation pattern of the AUT can be reconstructed using the self-correlation coefficient of the antenna pattern which can be measured in an RC. The proposed method only used the NLoS components, it can be considered as a generalized mode matching method which optimizes the SSH coefficients to match the measured self-correlation coefficients. This results in a system of nonlinear equations which can be solved/optimized using the well-developed Levenberg-Marquardt algorithm [29]. It has also been shown that the AR of an antenna can be measured in an efficient manner (rotated around one axis) in an RC. An overview of the framework of this novel method is shown in Fig. 30. Simulations and measurements have been conducted to verify the proposed theory. Error sources have been analyzed and quantified, and have been shown to be small for all of the cases considered in this paper.

REFERENCES

- [1] C. L. Holloway, H. A. Shah, R. J. Pirkel, W. F. Young, D. A. Hill and J. Ladbury, "Reverberation chamber techniques for determining the radiation and total efficiency of antennas," *IEEE Trans. Antennas Propagat.*, vol. 60, no. 4, pp. 1758-1770, Apr. 2012.
- [2] S. J. Boyes, P. J. Soh, Y. Huang, G. A. E. Vandenbosch and N. Khiabani, "Measurement and performance of textile antenna efficiency on a human body in a reverberation chamber," *IEEE Trans. Antennas Propagat.*, vol. 61, no. 2, pp. 871-881, Feb. 2013.
- [3] X. Chen, "On statistics of the measured antenna efficiency in a reverberation chamber," *IEEE Trans. Antennas Propagat.*, vol. 61, no. 11, pp. 5417-5424, Nov. 2013.
- [4] X. Chen, "Generalized statistics of antenna efficiency measurement in a reverberation chamber," *IEEE Trans. Antennas Propagat.*, vol. 62, no. 3, pp. 1504-1507, Mar. 2014.
- [5] Q. Xu, Y. Huang, X. Zhu, L. Xing, Z. Tian and C. Song, "A modified two-antenna method to measure the radiation efficiency of antennas in a reverberation chamber," *IEEE Antennas Wireless Propag. Lett.*, vol. 15, pp. 336-339, 2016.
- [6] P.-S. Kildal, C. Carlsson and J. Yang, "Measurement of free-space impedances of small antennas in reverberation chambers," *Microw. Opt. Technol. Lett.*, vol. 32, pp. 112-115, 2002.
- [7] P.-S. Kildal and K. Rosengren, "Correlation and capacity of MIMO systems and mutual coupling, radiation efficiency, and diversity gain of their antennas: Simulations and measurements in a reverberation chamber," *IEEE Commun. Mag.*, vol. 42, no. 12, pp. 104-112, Dec. 2004.
- [8] K. Rosengren and P.-S. Kildal, "Radiation efficiency, correlation, diversity gain and capacity of a six-monopole antenna array for a MIMO system: Theory, simulation and measurement in reverberation chamber," *Proc. Inst. Elect. Eng., Microw. Antennas Propag.*, vol. 152, no. 1, pp. 7-16, Feb. 2005.
- [9] P.-S. Kildal, K. Rosengren, J. Byun, and J. Lee, "Definition of effective gain and how to measure it in a reverberation chamber," *Microw. Opt. Technol. Lett.*, vol. 34, no. 1, pp. 56-59, Jul. 2002.
- [10] Q. Xu, Y. Huang, X. Zhu, S. S. Alja'afreh and L. Xing, "A new antenna diversity gain measurement method using a reverberation chamber," *IEEE Antennas Wireless Propag. Lett.*, vol. 14, pp. 935-938, 2015.
- [11] J. Koh, A. De, T. K. Sarkar, H. Moon, W. Zhao and M. S.-Palma, "Free space radiation pattern reconstruction from non-anechoic measurements using an impulse response of the environment," *IEEE Trans. Antennas Propag.*, vol. 60, no. 2, pp. 821-831, Feb. 2012.
- [12] V. Fiumara, A. Fusco, V. Matta, and I. M. Pinto, "Free-space antenna field-pattern retrieval in reverberation environments," *IEEE Antennas Wireless Propag. Lett.*, vol. 4, pp. 329-332, 2011.
- [13] P. Besnier, C. Lemonie, J. Sol and J.-M. Floc'h, "Radiation pattern measurements in reverberation chamber based on estimation of coherent and diffuse electromagnetic fields," in IEEE Conference on Antenna Measurements & Applications (CAMA), pp.1-4, 16-19 Nov. 2014.
- [14] C. Lemoine, E. Amador, P. Besnier, J.-M. Floc'h and A. Laisne, "Antenna directivity measurement in reverberation chamber from Rician K-factor estimation," *IEEE Trans. Antennas Propagat.*, vol. 61, no. 10, pp. 5307-5310, Oct. 2013.
- [15] M. Á. García-Fernández, D. Carsenat, and C. Decroze, "Antenna radiation pattern measurements in reverberation chamber using plane wave decomposition," *IEEE Trans. Antennas Propagat.*, vol. 61, no. 10, pp. 5000-5007, Oct. 2013.
- [16] M. Á. García-Fernández, D. Carsenat and C. Decroze, "Antenna gain and radiation pattern measurements in reverberation chamber using Doppler effect," *IEEE Trans. Antennas Propagat.*, vol. 62, no. 10, pp. 5389-5394, Oct. 2014.
- [17] H. Moussa, A. Cozza and M. Cauterman, "A novel way of using reverberation chambers through time reversal," in ESA Workshop on Aerospace EMC (ESA'09), pp. 10-2, Mar. 2009.
- [18] A. Cozza and A. Abou el-Aileh, "Accurate radiation-pattern measurements in a time-reversal electromagnetic chamber," *IEEE Antennas and Propagation Magazine*, vol. 52, no. 2, pp. 186-193, Apr. 2010.
- [19] F. Monsef, A. Cozza, P. Meteon and M. Djedidi, "Preliminary results on antenna testing in reverberating environments," in IEEE Conference on Antenna Measurements & Applications (CAMA), pp. 1-4, 16-19 Nov. 2014.
- [20] J. Jackson, *Classical Electrodynamics*. New York: Wiley, 1983.
- [21] Y. Chen and T. Simpson, "Radiation pattern analysis of arbitrary wire antennas using spherical mode expansions with vector coefficients," *IEEE Trans. Antennas Propagat.*, vol. 39, no. 12, pp. 1716-1721, Dec. 1991.
- [22] G. D. Galdo, J. Lotze, M. Landmann and M. Haardt, "Modelling and manipulation of polarimetric antenna beam patterns via spherical harmonics," in 14th European Signal Processing Conference, pp.1-5, 4-8 Sep. 2006.
- [23] J. Rahola, F. Belloni and A. Richter, "Modelling of radiation patterns using scalar spherical harmonics with vector coefficients," in 3rd European Conference on Antennas and Propagation (EuCAP), pp.3361-3365, 23-27 Mar. 2009.
- [24] M. Mhedhbi, S. Avrillon and B. Uguen, "Comparison of vector and scalar spherical harmonics expansions of UWB antenna patterns," in International Conference on Electromagnetics in Advanced Applications (ICEAA), pp.1040-1043, 9-13 Sep. 2013.
- [25] J. Yang, S. Pivnenko, T. Laitinen, J. Carlsson and X. Chen, "Measurements of diversity gain and radiation efficiency of the eleven antenna by using different measurement techniques," in 4th European

- Conference on Antennas and Propagation (EuCAP), pp.1-5, 12-16 Apr. 2010.
- [26] X. Chen, P. -S. Kildal and J. Carlsson, "Comparisons of different methods to determine correlation applied to multi-port UWB eleven antenna," in 5th European Conference on Antennas and Propagation (EuCAP), pp.1776-1780, 11-15 Apr. 2011.
- [27] Z. Gimbutas, L. Greengard, "A fast and stable method for rotating spherical harmonic expansions," *Journal of Computational Physics*, vol. 228, no. 16, pp. 5621-5627, 2009.
- [28] P. Hallbjorner, "Accuracy in reverberation chamber antenna correlation measurements," in International Workshop on Antenna Technology: Small and Smart Antennas Metamaterials and Applications (IWAT '07), pp.170-173, 21-23 Mar. 2007 .
- [29] D. W. Marquardt, "An algorithm for least-squares estimation of nonlinear parameters," *Journal of the Society for Industrial and Applied Mathematics*, vol. 11, no. 2, pp.431-441, 1963.
- [30] D. A. Hill, "Electronic mode stirring for reverberation chambers," *IEEE Trans. EMC*, vol. 36, no. 4, pp. 294-299, Nov. 1994.
- [31] P. -S. Kildal, C. Carlsson and J. Yang, "Measurement of free-space impedances of small antennas in reverberation chambers," *Microwave and Optical Technology Letters*, vol. 32, no. 2, pp. 112-115, Dec. 2001.
- [32] Y. Huang and D. J. Edwards, "A novel reverberating chamber: source-stirred chamber," in Proceeding of IEE 8th International Conference on EMC, pp. 120-124, Sep. 1992.
- [33] K. Rosengren, P. -S. Kildal, C. Carlsson and J. Carlsson, "Characterization of antennas for mobile and wireless terminals in reverberation chambers: improved accuracy by platform stirring," *Microwave and Optical Technology Letters*, vol. 39, no. 6, pp. 391-397, Sep. 2001.
- [34] IEEE Standard Test Procedures for Antennas, IEEE Std, 149-1979.
- [35] F. Jensen and A. Frandsen, "On the number of modes in spherical wave expansions," TICRA, Copenhagen, Denmark, Jan. 2005 [Online]. Available: <http://www.ticra.com>.